

Contrast Restoration of Weather Degraded Images

Srinivasa G. Narasimhan and Shree K. Nayar

Abstract—Images of outdoor scenes captured in bad weather suffer from poor contrast. Under bad weather conditions, the light reaching a camera is severely scattered by the atmosphere. The resulting decay in contrast varies across the scene and is exponential in the depths of scene points. Therefore, traditional space invariant image processing techniques are not sufficient to remove weather effects from images. In this paper, we present a physics-based model that describes the appearances of scenes in uniform bad weather conditions. Changes in intensities of scene points under different weather conditions provide simple constraints to detect depth discontinuities in the scene and also to compute scene structure. Then, a fast algorithm to restore scene contrast is presented. In contrast to previous techniques, our weather removal algorithm does not require any a priori scene structure, distributions of scene reflectances, or detailed knowledge about the particular weather condition. All the methods described in this paper are effective under a wide range of weather conditions including haze, mist, fog, and conditions arising due to other aerosols. Further, our methods can be applied to gray scale, RGB color, multispectral and even IR images. We also extend our techniques to restore contrast of scenes with moving objects, captured using a video camera.

Index Terms—Physics-based vision, atmosphere, bad weather, fog, haze, visibility, scattering, attenuation, airlight, overcast sky, scene structure, defog, dehaze, contrast restoration, shape from X, shape from weather, scene reconstruction.



1 TOWARD WEATHER-FREE VISION

HUMAN perception of scene color and contrast through the atmosphere has been extensively studied [14], [15], [17], [18]. For centuries, artists have rendered their paintings with an “atmospheric or aerial perspective” [7]. They illustrate, in their paintings, optical phenomena such as the bluish haze of distant mountains and reduced visibility under adverse weather conditions such as mist, fog, rain, and snow. Leonardo da Vinci’s paintings often contain an atmospheric perspective of the background scene [26], where farther scene points were painted brighter and bluer. While these optical phenomena can be argued to be aesthetically pleasing to humans, they are often hindrances to the satisfactory working of a computer vision system.

Most outdoor vision applications such as surveillance, terrain classification, and autonomous navigation require robust detection of image features. Under bad weather conditions, however, the contrast and color of images are drastically altered or degraded. Hence, it is imperative to remove weather effects from images in order to make vision systems more reliable. Unfortunately, the effects of bad weather increase exponentially with the distances of scene points from the sensor. As a result, conventional space invariant filtering techniques fail to adequately remove weather effects from images.

Recently, there has been an increased interest in the image processing and vision communities on issues related to imaging under bad weather. Kopeika [13] and Yitzhaky et al. [38] deblur atmospherically degraded

images using a weather-predicted atmospheric modulation transfer function, and an a priori estimate of the distance from which the scene is imaged. Oakley and Satherley [25] and Tan and Oakley [33], [34] describe a physics-based method to restore scene contrast without using predicted weather information. However, they assume that scene depths are known beforehand, and they approximate the distribution of radiances in the scene by a single Gaussian with known variance. Another work by Grewe and Brooks [9] uses wavelet-based fusion of multiple bad weather images to get a less blurred image.

Narasimhan and Nayar [21] analyze color variations in the scene under different weather conditions based on the dichromatic atmospheric scattering model proposed in [24]. Using constraints on scene color changes, they compute complete 3D structure and recover clear day scene colors from two or more bad weather images [23]. However, they assume that the atmospheric scattering properties do *not* change with the wavelength of light. This property holds over the visible spectrum only for certain weather conditions such as fog and dense haze. For several aerosols, however, scattering strongly depends on the wavelength of incident light. Furthermore, scene recovery using the dichromatic model is ambiguous for scene points whose colors match the color of fog or haze.

Polarization has been used as a cue to reduce haze in images based on the effects of scattering on light polarization [2], [5], [27]. In many works [4], [28], the radiation from the object of interest is assumed to be polarized, whereas the natural illumination scattered toward the observer (airlight) is assumed to be unpolarized. In other works [6], [29], [36], the radiation from the scene of interest is assumed to be unpolarized, whereas airlight is assumed to be partially polarized. Polarizing filters are, therefore, used widely by photographers to reduce haziness in landscape images, where the radiance from the landscapes is generally unpolarized.

• The authors are with the Computer Science Department, Columbia University, 500 West 120th Street, Room 450, New York, NY 10027. E-mail: {srinivas, nayar}@cs.columbia.edu.

Manuscript received 6 Feb. 2002; revised 25 Sept. 2002; accepted 4 Oct. 2002. Recommended for acceptance by R. Beveridge.

For information on obtaining reprints of this article, please send e-mail to: tpami@computer.org, and reference IEEECS Log Number 115843.

However, polarization filtering alone does not ensure complete removal of haze. Schechner et al. [29], [30] further analyzed two or more polarization filtered images to compute scene structure and dehaze images. The effectiveness of polarization as a cue to remove weather effects is limited under dense fog and mist with overcast sky illumination since scattered light is mostly depolarized.

In this paper, we present a physics-based method to restore contrast of a scene from two or more images taken in uniform bad weather conditions. A monochrome atmospheric scattering model that describes how scene intensities are affected by homogeneous weather conditions is presented. This model is valid in both the visible and near-IR spectra, and for a wide range of weather conditions such as mist, haze, fog, and other aerosols. The model does not require the scattering properties of the atmosphere to be constant with respect to wavelength of light over a large spectral range (for example, the range of visible spectrum, as in [23]). Since we are interested in a short range of distances (of the order of a few kilometers), we assume that the weather condition does not change spatially in the field of view.¹

Using the monochrome weather model, we show how contrast of a scene degrades with distance. We conclude that standard contrast enhancement techniques can only handle a scene or a region within a scene at a fixed distance from the sensor. A simple contrast restoration technique similar to contrast stretching is derived for scenes where depth segmentation is known a priori. Changes in scene intensities, observed under different weather conditions, present strong physical constraints regarding scene structure. These constraints are exploited to automatically detect depth discontinuities in the scene and also to recover complete scene structure from two images taken under different weather conditions during daytime. Using the computed structure, contrast is restored from a single weather-degraded image of the scene. Unlike previous methods for contrast restoration, we do not need accurately predicted weather information or prior distributions on scene radiances. We extend our algorithms to handle video and describe a simple heuristic to restore contrasts of moving objects in the scene whose depths are unknown.

The entire analysis in this paper is done for monochrome (single narrow spectral band) images. However, the same methods can be applied independently to images with multiple spectral bands. We show that our methods can be applied to images taken using gray scale, wide-band RGB, multispectral, and also narrow-band IR cameras.

2 ATMOSPHERIC SCATTERING MODELS

Scattering of light by physical media has been one of the main topics of research in the atmospheric optics and astronomy communities. In general, the exact nature of scattering is highly complex and depends on the types, orientations, sizes, and distributions of particles constituting the media, as well as wavelengths, polarization states, and directions of the incident light [3], [10]. Here, we focus on two models—attenuation and airlight, which form the basis of our work. Since we are interested in a short range of

distances (of the order of a few kilometers), we assume that the properties of the weather condition (say, type of particles and their density) does not change spatially. In other words, we only consider homogeneous atmospheres in this paper. Also, given the limited dynamic range of the sensors (say, 8 bits per pixel), we do not explicitly model multiple scattering or blurring effects of bad weather [23].

2.1 Attenuation and Airlight

The attenuation model describes the way light gets attenuated as it traverses from a scene point to the observer. Due to atmospheric scattering, a fraction of light flux is removed from the incident beam. The unscattered flux, called direct transmission, is transmitted to the observer. The attenuated irradiance at the observer is given by (see [17], [21]),

$$E_{dt}(d, \lambda) = \frac{E_{\infty}(\lambda) r(\lambda) e^{-\beta(\lambda)d}}{d^2}, \quad (1)$$

where, d is the depth of the scene point from the observer and λ is the wavelength. $\beta(\lambda)$ is called the *scattering coefficient* of the atmosphere; it represents the ability of a unit volume of atmosphere to scatter light in all directions. $\beta(\lambda)d$ is called the *optical depth* of the scene point. E_{∞} is the *horizon brightness* and r is a function that describes the reflectance properties and the sky aperture² of the scene point. The attenuated irradiance is illustrated by the solid arrow from the scene to the sensor in Fig. 1. The sky is assumed to be mostly cloudy or overcast and that the radiance from the sky varies smoothly with respect to the polar and azimuth angles of the hemisphere [8], [11], [20]. For more details, we refer the reader to [21].

The second atmospheric scattering model we consider is called the *airlight* model. The airlight model quantifies how a column of atmosphere acts as a light source by reflecting environmental illumination towards an observer. Refer to the dotted arrows in Fig. 1. The light reflected into the line of sight is integrated along the entire path length, d , from the scene to the observer. Then, the irradiance due to airlight is given by (see [16]),

$$E_a(d, \lambda) = E_{\infty}(\lambda) \left(1 - e^{-\beta(\lambda)d}\right). \quad (2)$$

The total irradiance E received by the sensor is the sum of irradiances due to attenuation and airlight, respectively,

$$E(d, \lambda) = E_{dt}(d, \lambda) + E_a(d, \lambda). \quad (3)$$

2.2 Wavelength Dependence of Scattering

Generally, different wavelengths of light are scattered differently by atmospheric particles. Interesting atmospheric phenomena such as the blueness of the sky and the bluish haze of distant mountains are examples of the wavelength selective behavior of atmospheric scattering [12], [18]. In these cases, the blue wavelengths are scattered more compared to other visible wavelengths. On the other hand, fog and dense haze scatter all visible wavelengths more or less the same way.

Over the visible spectrum, Rayleigh's law of atmospheric scattering provides the relationship between the scattering coefficient β and the wavelength λ [16]:

2. Solid angle subtended by the area of sky visible to a scene point.

1. Multiple scattering effects are not taken into account in this model and hence, for highly dense weather conditions, the model will not be effective. Also, this model does not take into account blurring effects of bad weather due to turbulence.

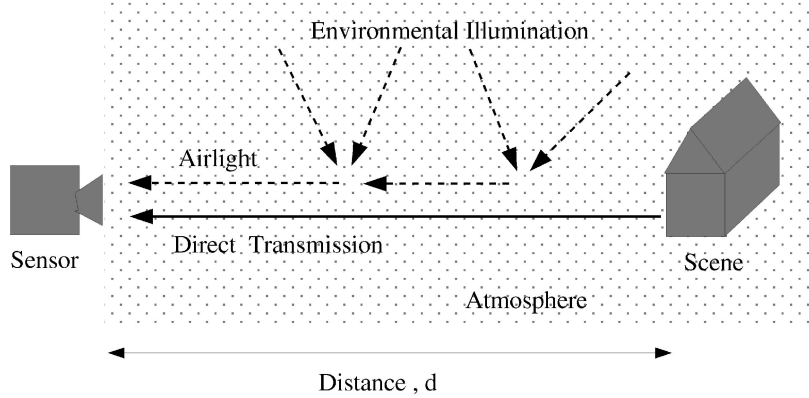


Fig. 1. Scattering of light by atmospheric particles can be described by two models—direct transmission (or attenuation) and airlight. Direct transmission is the attenuated irradiance received by the sensor from the scene point along the line of sight. Airlight is the total amount of environmental illumination (sunlight, skylight, ground light) reflected into the line of sight by atmospheric particles.

$$\beta(\lambda) \propto \frac{1}{\lambda^\gamma}, \quad (4)$$

where $0 \leq \gamma \leq 4$ depending on the exact particle size distribution in the atmosphere. For pure air, the constituent particle (molecules) sizes are very small compared to the wavelength of light and hence, there is a strong wavelength dependence of scattering. In this case, $\gamma = 4$; short (blue) wavelengths dominate and we see the clear blue sky. For fog, the constituent particle (water droplets) sizes are large compared to the wavelength of light and, hence, the scattering coefficient does not depend on wavelength. So, for fog, $\gamma \approx 0$; all wavelengths are scattered equally and we see grayish (or white) fog. A wide gamut of atmospheric conditions arise from aerosols whose particle sizes range between minute air molecules ($10^{-4} \mu m$) and large fog droplets ($1 - 10 \mu m$). Such aerosols (e.g., mild haze) show a significant wavelength selectivity ($0 < \gamma < 4$).

2.3 Weather Conditions and Camera Response

Different cameras measure irradiance over different color bands. Some examples include gray-scale cameras (entire visible spectrum), conventional color cameras (three broad bands R, G, and B), and multispectral cameras (multiple narrow color bands). In the appendix, we derive an expression for the brightness recorded by a monochrome (narrow spectral band) camera, using (3). In this derivation, we assume that the scattering coefficient β remains constant within the spectral bandwidth of the monochrome camera.

Keeping the above assumption in mind, we now discuss under what weather conditions can our methods be applied to various sensors. Recall from Section 2.2 that the scattering coefficient for fog and dense haze remains more or less constant over the visible spectrum. Accordingly, a broadband RGB or gray-scale camera suffices to analyze images taken in fog and dense haze. For other aerosols such as mild haze, multispectral cameras or cameras fitted with narrow-band filters should be used in order to apply our methods satisfactorily. Finally, scattering coefficients of most weather conditions vary significantly in the near-IR spectrum [37] and hence, narrow-band IR cameras have to be used for the analysis beyond the visible wavelengths. In other words, the greater the variation in the scattering coefficient with respect

to wavelength, the narrower the spectral bandwidth needed for effective results.

We would like to clarify that multiple color channels are not required for our algorithms. We can, however, apply the methods we describe in this paper to each color channel of the sensor independently. This is in contrast to previous methods that required at least three color channels (say, R, G, and B) over which the scattering coefficient had to be equal [21].

3 CONTRAST DEGRADATION IN BAD WEATHER

In this section, we show how contrast degrades in poor visibility conditions as a function of both the scattering coefficient of the atmosphere and the distance of the scene from the sensor. Consider an image taken in bad weather. The brightness at any pixel recorded by a monochrome camera is derived in the appendix:

$$E = I_\infty \rho e^{-\beta d} + I_\infty (1 - e^{-\beta d}), \quad (5)$$

where I_∞ is termed as sky intensity. We call ρ the *normalized radiance* of a scene point; it is a function of the scene point reflectance (BRDF), normalized sky illumination spectrum, and the spectral response of the camera, *but not* the weather condition defined by (β, I_∞) (see the appendix).

Using (5), we formulate the image contrast between two adjacent scene points as a function of the amount of scattering and their distance from the observer. Consider two adjacent scene points P_i and P_j at the same depth d from a sensor. Their pixel intensities are given by,

$$\begin{aligned} E^{(i)} &= I_\infty \rho^{(i)} e^{-\beta d} + I_\infty (1 - e^{-\beta d}), \\ E^{(j)} &= I_\infty \rho^{(j)} e^{-\beta d} + I_\infty (1 - e^{-\beta d}). \end{aligned} \quad (6)$$

The observed contrast between P_i and P_j can be defined as,

$$\frac{E^{(i)} - E^{(j)}}{E^{(i)} + E^{(j)}} = \frac{\rho^{(i)} - \rho^{(j)}}{\rho^{(i)} + \rho^{(j)} + 2(e^{\beta d} - 1)}. \quad (7)$$

This shows that the contrast degrades *exponentially* with the scattering coefficient β and the depths of scene points in bad weather. As a result, conventional space-invariant image processing techniques cannot be used to completely remove

weather effects. Note that other formulations for image contrast (e.g., MTF, log intensity) [13] can also be used to illustrate the exponential contrast decay.

4 CONTRAST RESTORATION OF ISO-DEPTH REGIONS

We now describe a simple method to restore scene contrast from one bad weather image using depth segmentation of the scene. We define depth segmentation as the extraction of iso-depth regions in the scene. Note, this does *not* mean that actual scene depths have to be known. In several situations, it may be easy to interactively provide the necessary segmentation. For instance, in urban scenes with frontal views of buildings, a user can easily mark out regions that roughly have the same depths. Later, we will present two automatic depth segmentation techniques using images taken under different weather conditions.

Consider an image taken in bad weather. The brightness at any pixel recorded by a monochrome camera is given by,

$$E = I_\infty \rho e^{-\beta d} + I_\infty (1 - e^{-\beta d}). \quad (8)$$

Now, consider two scene points P_i and P_j at the same depth d from a sensor. The observed contrast between P_i and P_j is given by (7). Eliminating the unknown $e^{-\beta d}$ from (6), we obtain,

$$\frac{1 - \rho^{(i)}}{1 - \rho^{(j)}} = \frac{I_\infty - E^{(i)}}{I_\infty - E^{(j)}}. \quad (9)$$

For robustness, we consider all the pixels at the same depth,

$$\frac{1 - \rho^{(i)}}{\sum_j (1 - \rho^{(j)})} = \frac{I_\infty - E^{(i)}}{\sum_j (I_\infty - E^{(j)})}. \quad (10)$$

Then, the normalized radiance of any scene point is obtained using,

$$\rho^{(i)} = 1 - \left(\sum_j 1 - \sum_j \rho^{(j)} \right) \frac{I_\infty - E^{(i)}}{\sum_j (I_\infty - E^{(j)})}. \quad (11)$$

This procedure is repeated independently for each depth in the scene. So, if we have a priori depth segmentation of the scene and have measured the sky intensity I_∞ , then $\rho^{(i)}$ can be computed up to a linear factor $\sum_j \rho^{(j)}$. Since ρ is independent of the weather condition, we have restored the contrast of the scene using just *one* bad weather image.

What can we do if we do not have the sky intensity I_∞ ? Let us assume that P_j has the minimum brightness within the iso-depth scene points: $E^{(j)} = E^{\min}$. Also, since scene point brightnesses are much lower than sky brightness on an overcast day, i.e., $(\forall i), I_\infty > E^{(i)}$, we can set $I_\infty = E^{\max}$. Then, the right-hand side of (9) is just contrast stretching the inverted bad weather image. In other words, by setting $\rho^{\min} = 0$ and $\rho^{\max} = 1$, contrast stretching (or histogram stretching) each iso-depth region in the image can restore contrast. Even though contrast is restored at each depth satisfactorily, the image can look unrealistic. In summary, simple image processing techniques such as contrast stretching can be effective for scenes that are at the same depth from the sensor (e.g., a planar scene at a fixed distance from the camera). Clearly, for scenes with

significant depth variations, this simple method will not be effective.

5 DEPTH EDGES FROM TWO WEATHER CONDITIONS

In this section, we present a simple cue to automatically locate the depth edges (discontinuities) present in a scene from two monochrome images taken under different but unknown weather conditions. In other words, we present a method to label image edges as reflectance edges and depth edges. Several researchers have pursued the problem of classifying different types of edges (diffuse, specular, and occluding) based on image intensity/color cues [31], [35] and polarization cues [1]. As we shall show, changes in weather conditions can be exploited as a cue to differentiate depth edges from reflectance edges.

Note that closed contours of depth edges can be used for depth segmentation. In outdoor surveillance applications, video cameras capture the same scene (albeit with moving objects) over long periods of time during which the weather may change. Also, depth edges in the static portion of any scene have to be computed just once and not for every video frame. Hence, we see this as an initialization step that needs to be done before applying the contrast restoration algorithm of Section 4 to all frames.

Consider a small image neighborhood corresponding to scene points that are at the same depth from an observer (i.e., no depth edges present). We call such a neighborhood an *iso-depth neighborhood*. From (5), the average brightness of an iso-depth neighborhood is,

$$\bar{E} = [I_\infty e^{-\beta d}] \bar{\rho} + [I_\infty (1 - e^{-\beta d})], \quad (12)$$

and the standard deviation of the neighborhood is,

$$\sigma_E = \sqrt{\frac{1}{n} \sum_{i=1}^n (E^{(i)} - \bar{E})^2}. \quad (13)$$

Using (5), we simplify to obtain,

$$\sigma_E = I_\infty e^{-\beta d} \sqrt{\frac{1}{n} \sum_{i=1}^n (\rho^{(i)} - \bar{\rho})^2}. \quad (14)$$

Normalizing the pixel values in the neighborhood, we get,

$$\frac{E^{(i)} - \bar{E}}{\sigma_E} = \frac{(\rho^{(i)} - \bar{\rho})}{\sqrt{\frac{1}{n} \sum_{i=1}^n (\rho^{(i)} - \bar{\rho})^2}}. \quad (15)$$

For iso-depth neighborhoods, clearly the above equation is *invariant* to the weather condition (β, I_∞) . More importantly, the invariance does *not* hold for a neighborhood that contains depth edges. This is easily explained as follows: The airlight does not remain constant across a neighborhood with depth discontinuities. Hence, subtracting the mean (as in (15)) will not remove the airlight completely.

Now, let us consider two images captured under different weather conditions. We assume that the two images are taken under similar daylight distributions. However, the magnitudes of the distributions (I_∞) may vary. In other words, the shadow edges (if any) appear at the same pixel

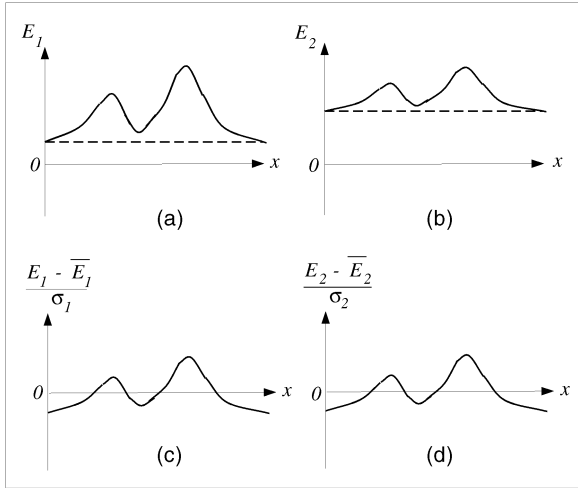


Fig. 2. Invariance of iso-depth neighborhoods to weather conditions. (a) and (b) Signals representing the intensities of a neighborhood of iso-depth scene points in two weather conditions. Airlight (dashed lines) is constant for the entire neighborhood. (c) and (d) Normalized signals in the two weather conditions match exactly.

location in both the images. Figs. 2a and 2b illustrate the brightnesses within an iso-depth neighborhood under two weather conditions. Figs. 2c and 2d show that the normalized signals under the two weather conditions match perfectly. On the other hand, Fig. 3 illustrates that normalized signals of scene neighborhoods that contain depth edges, do not match. Normalized SSD can be used to determine the quality of the match. Note that (15) still holds if we apply a more robust estimate of mean and standard deviation (for e.g., median of absolute deviations from the neighborhood median).

It is interesting to note what happens if we treat the entire image as a single neighborhood. Applying normalized SSD to two images of a scene, a poor match implies that the weather condition *changed between* the two images and a good match

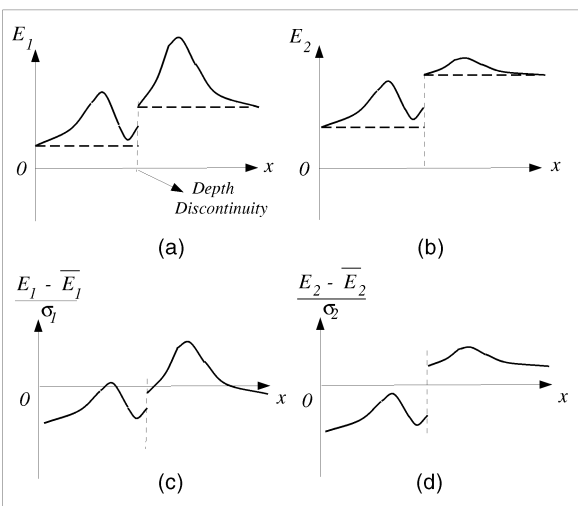


Fig. 3. Illustration of scene intensities of a neighborhood that has a depth edge. (a) and (b) Signals representing the intensities of the neighborhood under two weather conditions. Airlight (dashed lines) *varies* across the neighborhood. (c) and (d) Normalized signals in the two weather conditions do not match.

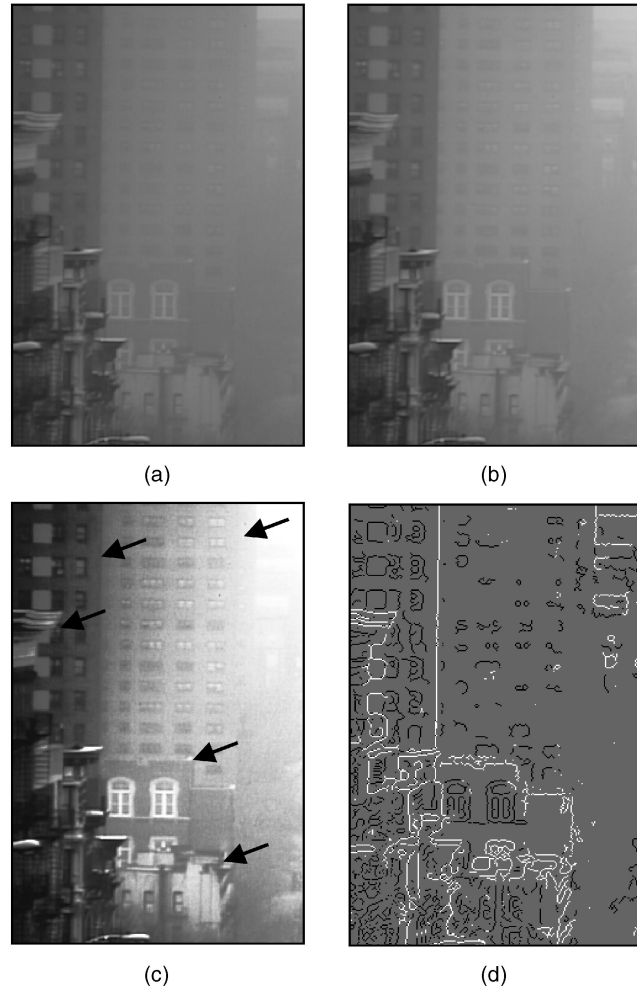


Fig. 4. Classification of image edges into reflectance edges and depth edges. (a) and (b) Images of the same scene captured under different fog conditions (half an hour apart). (c) The image in (a) is histogram equalized to aid visualization of depth edges (shown using arrows). (d) White pixels denote depth edges and black pixels denote reflectance edges. Note that the edge detector was applied to the original image in (a) and not the histogram equalized image in (c).

implies otherwise. For this, the scene should have at least two different depths and the images should be linearized using the radiometric response function of the camera. This cue is helpful in deciding which frames can be used to compute depth edges in a video sequence.

Fig. 4 shows the experimental results of classifying image edges into *reflectance edges* and *depth edges* for a real scene captured under two different foggy conditions. The time between the capture of the images was about half an hour. The edge map of one of the images was computed using the Canny edge detector. For each edge pixel, we considered 15×15 neighborhoods around the pixel in the two images. We applied normalized SSD to match these neighborhoods. For the depth edges, the normalized SSD value was high; for the reflectance edges, the value was low. The depth edges are shown in white and reflectance edges are shown in black (Fig. 4d). Note if both reflectance edges and depth edges are within the same neighborhood, this method may misclassify the reflectance edges as depth edges. Also, note that shadow edges (if any) will not be distinguished from

reflectance edges. Finally, this method to classify edges can be sensitive to noise, especially under poor weather conditions. Under poor weather conditions, due to the limited dynamic range of the sensor (typically 8 bits), the direct transmission (signal) to airlight (noise) ratio can be so low that the direct transmission magnitude can be compared to the sensor noise level. In this case, the results produced by the method may not be trusted.

6 SCENE STRUCTURE FROM TWO WEATHER CONDITIONS

In the previous section, we described a method to locate depth discontinuities from two bad weather images. Note, however, that normalized SSD is effective only in textured neighborhoods (reflectance edges and depth discontinuities). In other words, normalized SSD is not reliable for “flat” intensity regions and regions where depth changes are *gradual*. Moreover, due to the blurring seen in images taken under *poor* visibility conditions, the edge maps may not be reliable enough to create closed contours of depth discontinuities (needed for depth segmentation).

In this section, we present a method to compute complete structure of an arbitrary scene, from two images taken under different weather conditions. In contrast to the methods proposed in [21], [24] that *require* color images (three color channels), our algorithm can be applied to both gray scale as well as color images.

Consider the observed pixel values E_1 and E_2 of a scene point under two weather conditions (β_1, I_{∞_1}) and (β_2, I_{∞_2}) . Let us examine how the brightness of this scene point changes from the first weather condition to the second. From (5),

$$\begin{aligned} E_1 &= I_{\infty_1} \rho e^{-\beta_1 d} + I_{\infty_1} (1 - e^{-\beta_1 d}) \\ E_2 &= I_{\infty_2} \rho e^{-\beta_2 d} + I_{\infty_2} (1 - e^{-\beta_2 d}). \end{aligned} \quad (16)$$

Eliminating ρ from (16) we get,

$$E_2 = \left[\frac{I_{\infty_2}}{I_{\infty_1}} e^{-(\beta_2 - \beta_1)d} \right] E_1 + \left[I_{\infty_2} (1 - e^{-(\beta_2 - \beta_1)d}) \right], \quad (17)$$

which is *linear* in E_1 and E_2 . Also, for the two weather conditions, the coefficients of the linear equation depend *only* on scene depth. In other words, for iso-depth scene points, the plot of E_1 versus E_2 is a straight line.

Another significant constraint results from our physical model that suggests a means of estimating sky intensities. Interestingly, if we substitute $E_1 = I_{\infty_1}$ in (17), we get $E_2 = I_{\infty_2}$, irrespective of the depth d . Therefore, the point $(I_{\infty_1}, I_{\infty_2})$ lies on all the straight lines corresponding to different depths in the scene (see Fig. 5). In other words, the intersection of straight lines corresponding to different depths yields the sky intensities I_{∞_1} and I_{∞_2} .

The iso-depth lines in the plot of E_1 versus E_2 can be detected using the Hough transform. Then, the intersection (sky intensities) of the iso-depth lines can be computed using a least squares line-fitting algorithm. A problem arises if the iso-depth lines are not detected correctly in the plot of E_1 versus E_2 . In other words, scene depths can change smoothly and the iso-depth lines could “bunch up.” In order to

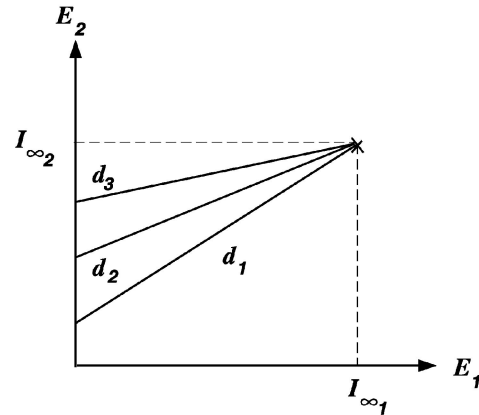


Fig. 5. Plot of the pixel values E_1 observed under one weather condition versus the corresponding pixel values E_2 observed under another weather condition. Each line represents all the scene points at the same depth from the sensor. All iso-depth lines intersect at the horizon brightnesses $(I_{\infty_1}, I_{\infty_2})$ of the two weather conditions.

compute sky intensities, we just divide the two images into blocks and within each block we fit lines to the (E_2, E_1) pairs of scene points. If the fit is good, we decide that the scene points in the block are at the same depth. Finally, we use at least two such iso-depth blocks to estimate sky the intensities.

Substituting the values of I_{∞_1} and I_{∞_2} in (17), we obtain the scaled depth of *each* scene point:

$$(\beta_2 - \beta_1)d = - \ln \frac{I_{\infty_2} - E_2}{I_{\infty_1} - E_1} - \ln \frac{I_{\infty_1}}{I_{\infty_2}}. \quad (18)$$

Thus, we have computed the depth map of a scene from two images taken under different weather conditions.

7 CONTRAST RESTORATION USING SCENE STRUCTURE

In Section 4, we described a method to restore scene contrast given a depth segmentation of the scene. This method is simple and effective for scenes where depth changes are abrupt (for example, an urban scene with frontal views of buildings). However, it is hard to define good depth segmentation when scene depths change *gradually* (for instance, a natural scene with mountains or an urban scene with an oblique view of a road). In this section, we present a method to restore contrast of an *arbitrary* scene using *scaled depths* (18) of scene points.

We assume that there exists a patch E_{zero} in the scene whose direct transmission is zero. This can happen in two instances. First, E_{zero} can be a black patch with its scene radiance equal to zero. Note that the black scene patch will not appear black in the image due to the addition of airlight. Second, E_{zero} could be a distant scene patch that is completely invisible due to strong airlight. In other words, this distant scene patch has zero direct transmission and its contrast cannot be restored from a bad weather image.

We can either mark such a patch manually or detect one automatically from the image. To detect zero direct transmission patches automatically in weather degraded images, we use the method described in [21]. Since the

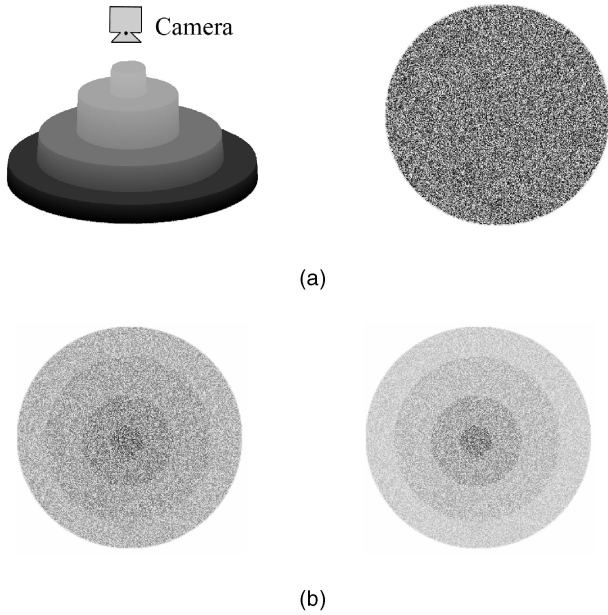


Fig. 6. Generating a synthetic scene—a stack of discs textured with random gray dots. (a) On the left is the 3D structure and on the right is an image of the top view of the scene. The gray levels on the structure are used only to illustrate the disks better. (b) Two different amounts of fog and noise ($\sigma = 3.0$ gray levels) are added to the image in (a).

apparent brightness of the patch E_{zero} is solely due to airlight, its optical depth can be computed as,

$$\beta d_{zero} = -\ln(1 - E_{zero}/I_{\infty}). \quad (19)$$

Then, the optical depth of *any other* scene point P_i is obtained using,

$$\beta d_i = (\beta d_{zero}) \left(\frac{d_i}{d_{zero}} \right), \quad (20)$$

where the second term can be computed using the ratio of scaled depths (see (18)). Then, the normalized radiance ρ_i of the scene point P_i is estimated using (5). Recall that ρ does not depend on the weather condition (β, I_{∞}). Thus, by computing ρ for each scene point, we restore contrast of the entire scene.

Note that structure computation requires two images to be taken under different weather conditions, but under similar daylight spectra. However, once scene structure is computed, contrast can be restored from a single image of the scene taken under arbitrary weather and illumination conditions.

8 EXPERIMENTAL RESULTS

We performed experiments with both synthetic and real scenes. Fig. 6a shows a synthetic scene consisting of a stack of cylinders with random brightness values. To this image, two different amounts of fog are added according to the model described in (5). To this image, Gaussian random noise of $\sigma = 3.0$ gray levels was added. Figs. 7a and 7b shows the results of applying the structure computation and contrast restoration algorithms to images of the synthetic scene. The error in the recovered depth map was less than 1 percent.

Results of experiments performed on images of real scenes are shown in Figs. 8 and 9. The images were captured

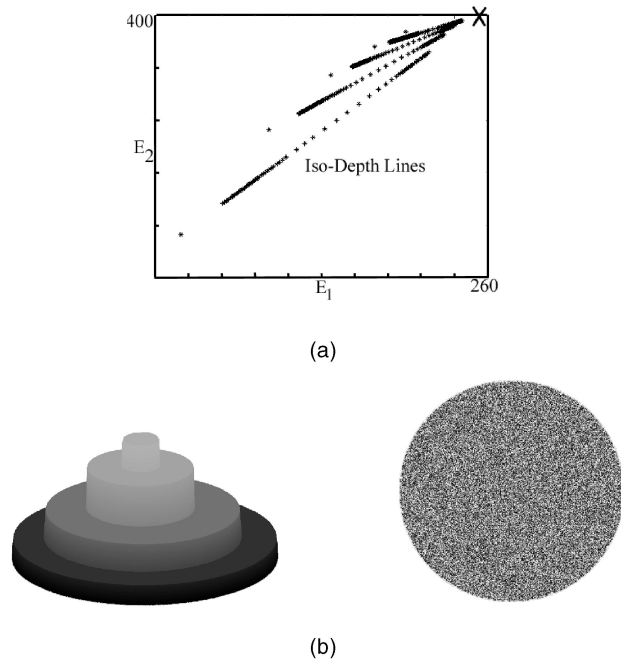


Fig. 7. Experiments on a synthetic scene—a stack of discs textured with random gray dots. Two images of a synthetic scene with different amounts of fog are shown in Fig. 6b. (a) Iso-depth lines shown in the plot of pixel values under the first weather condition versus the corresponding pixel values under the second weather condition. X mark shows the intersection $(I_{\infty_2}, I_{\infty_1})$ of all the iso-depth lines. (b) The recovered structure and contrast restored image. Compare (b) with the original synthetic scene in Fig. 6a.

using a Professional KODAK DCS 315 digital camera. Multiple exposures of the same scene were acquired and the radiometric response function of the camera was computed using the method proposed in [19]. Then, the multiple exposed images were linearized and combined using simple weighted averaging to obtain a high dynamic range image of the scene. Fig. 8a shows two high dynamic range images of the same scene captured under different conditions of mist (light and moderate). The depth map computed using the algorithm mentioned in Section 6 is shown in Fig. 8b. The mist was removed using the contrast restoration algorithm mentioned in Section 7. Notice the windows of the farther buildings that are clearly visible in Fig. 8d as compared to the images in Fig. 8a.

We performed experiments under rainy conditions also. Since we are interested in a far away scene, the captured image does seem like a foggy or a misty one due to spatio-temporal averaging in the sensor. The results proved that we can apply our algorithm to rainy images of faraway scenes as well. In this case, we just captured one image under mild rain conditions shown in Fig. 9a. The depth map, precomputed from the misty images shown in Fig. 8a, was used to restore the contrast of the rainy day image. Thus, changes in weather conditions are required only to compute scene structure whereas contrast restoration can be applied to a single image of that scene taken under arbitrary weather conditions. Compare the results of our algorithm (Fig. 9d) with conventional histogram equalization (Fig. 9b).

In general, removing the spatio-temporal effects of rain is a much harder problem compared to more stable weather

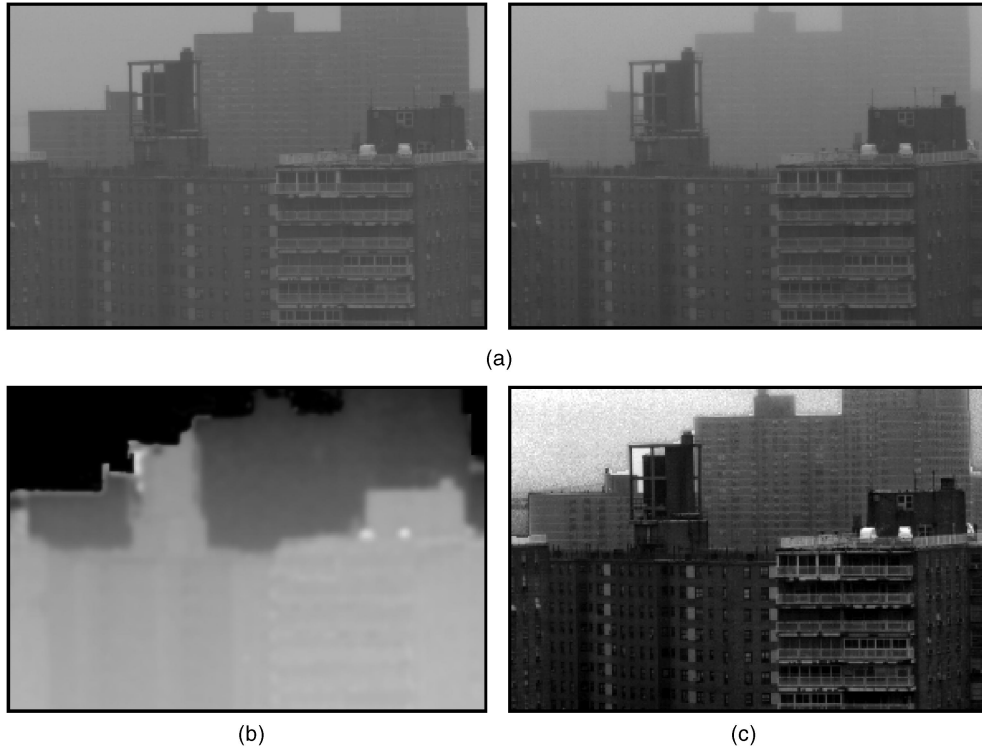


Fig. 8. Structure computation and restoration of image contrast from two images taken under poor visibility conditions. The depth map is median filtered and averaged to reduce noise. Notice the significant increase in contrast in the farther buildings. Contrast stretching is applied to all the images for display purposes. (a) Images taken at 3 P.M. and 4 P.M. under poor visibility conditions (mist). (b) Computed depth map. (c) Contrast restore image.

conditions such as fog, mist, and haze. The brightnesses due to raindrops in the scene cannot be modeled using the simple direct transmission and airlight models used in this paper.

8.1 Experiments with Video: Moving Objects

Consider an outdoor surveillance video camera capturing a scene (with moving objects) over an extended period of time. We would like to process this video in real-time to obtain a weather-free video. Note that our algorithms cannot remove temporal effects of rain from a video of a rainy scene. For the purposes of discussion, we define the static part of the scene as the *background* and the moving objects in the scene as the *foreground*. The foreground objects can be separated from the background using any background subtraction method (for instance, [32]). Then, weather-free video is obtained using an algorithm that has the following two stages:

- **Initialization stage.** We first detect any change in weather condition using normalized SSD (Section 5). Then, the two frames that correspond to the different weather conditions are used to compute scaled depths of the background scene (Section 6).
- **Contrast Restoration.** Note that the methods we described hitherto cannot be used to restore contrast of moving objects since their depths are unknown. Therefore, heuristics are needed to assign depths to foreground objects. One conservative heuristic is to examine the depths in a neighborhood around each moving object and assign the minimum depth to it.

The algorithm presented in Section 7 can then be applied to the entire frame to restore scene contrast.

Experimental results with a video of a traffic scene taken under foggy conditions are shown in Fig. 10. We used an off-the-shelf 8-bit digital video camera and captured two short video clips half an hour apart. As described in previous experiments, we linearized the frames with the radiometric response function of the video camera. We averaged 100 frames in each video clip to reduce noise and used the resulting images to compute structure of the background scene (buildings). The scaled depths in the road region were linearly interpolated using scaled depth values at pixels on the left and right corners of the road. Then, contrasts of buildings, the road, and moving vehicles were restored for each frame of the video. Notice the significant increase in contrast at various depths in the scene (Figs. 10d and 11). Compare our method to histogram equalization in Fig. 12. In our current implementation, contrast restoration was applied to the video offline.

9 SUMMARY

In this paper, we addressed the problem of restoring the contrast of atmospherically degraded images and video. We presented methods to locate depth discontinuities and to compute structure of a scene, from two images captured under different weather conditions. Using either depth segmentation (regions within closed contours of depth edges)

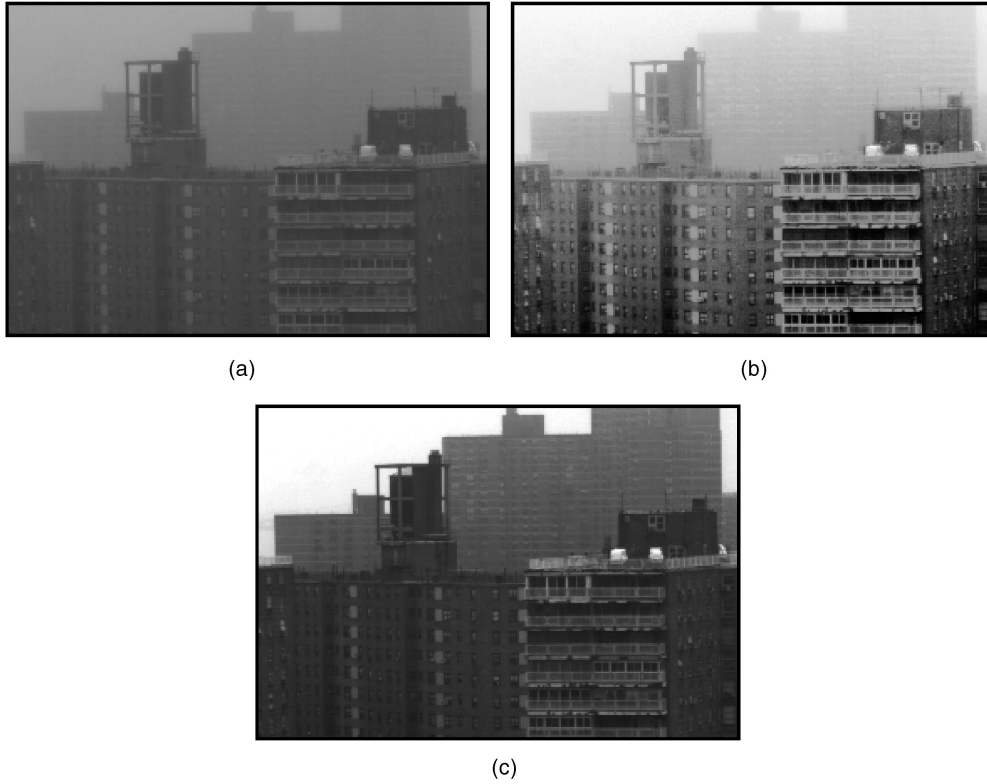


Fig. 9. Contrast restoration from one bad weather (in this case, rain) image and precomputed scene structure. Scene structure can be computed using two images taken under possibly different weather conditions (say, mist). The depth map computed from two misty images (Fig. 8a) was used to restore contrast from just one image of the same scene under rain. The rainy image shown in (a) and the misty images shown in Fig. 8a were captured on different days. (b) Applying histogram equalization to the entire rainy image does not enhance contrast in all depths. (c) Contrast restoration using the algorithm proposed in Section 7.

or scene structure (scaled depths), we then showed how to restore contrast from any image of the scene taken in bad weather. Note, although structure computation requires changes in weather, the contrast restoration algorithms do not. The entire analysis is presented for monochrome images. However, our methods can be applied to images captured using multispectral cameras, IR cameras, and the usual broadband RGB and gray-scale cameras.

APPENDIX

MONOCHROME CAMERA SENSING IN BAD WEATHER

In this section, we derive an expression for the intensity E , of a scene point under bad weather, recorded by a camera within a narrow wavelength band $(\lambda, \lambda + \delta\lambda)$. From (3) we write,

$$E = \int_{\lambda}^{\lambda+\delta\lambda} s(\lambda)(E_{dt}(d, \lambda) + E_a(d, \lambda)) d\lambda, \quad (21)$$

where $s(\lambda)$ is the spectral response of the camera. We assume that the scattering coefficient β does not change appreciably over the narrow spectral band and write,

$$E = \frac{e^{-\beta d}}{d^2} \int_{\lambda}^{\lambda+\delta\lambda} E_{\infty}(\lambda)s(\lambda)r(\lambda)d\lambda \dots + (1 - e^{-\beta d}) \int_{\lambda}^{\lambda+\delta\lambda} E_{\infty}(\lambda)s(\lambda)d\lambda. \quad (22)$$

The sky illumination spectrum can be written as,

$$E_{\infty}(\lambda) = I'_{\infty} \hat{E}_{\infty}(\lambda), \quad (23)$$

where I'_{∞} is the magnitude of the sky illumination spectrum and $\hat{E}_{\infty}(\lambda)$ is the normalized sky illumination spectrum. Letting

$$g = \int_{\lambda}^{\lambda+\delta\lambda} \hat{E}_{\infty}(\lambda)s(\lambda)d\lambda, \quad (24)$$

$$\rho = \frac{1}{gd^2} \int_{\lambda}^{\lambda+\delta\lambda} \hat{E}_{\infty}(\lambda)s(\lambda)r(\lambda)d\lambda,$$

$$I_{\infty} = I'_{\infty}g,$$

we rewrite the final brightness at any pixel as,

$$E = I_{\infty} \rho e^{-\beta d} + I_{\infty} (1 - e^{-\beta d}), \quad (25)$$

where I_{∞} is termed as sky intensity. Note that ρ is a function of normalized sky illumination spectrum, scene point reflectance, and the spectral response of the camera, *but not* the weather condition β . The algorithm we present in the paper recovers ρ for each pixel to restore scene contrast.

Let us now examine the wavelength range in which this model can be applied. By changing the limits of integration to $[\lambda_1, \lambda_2]$, and assuming the scattering coefficient to be constant over this wavelength band, we can use the same model for a

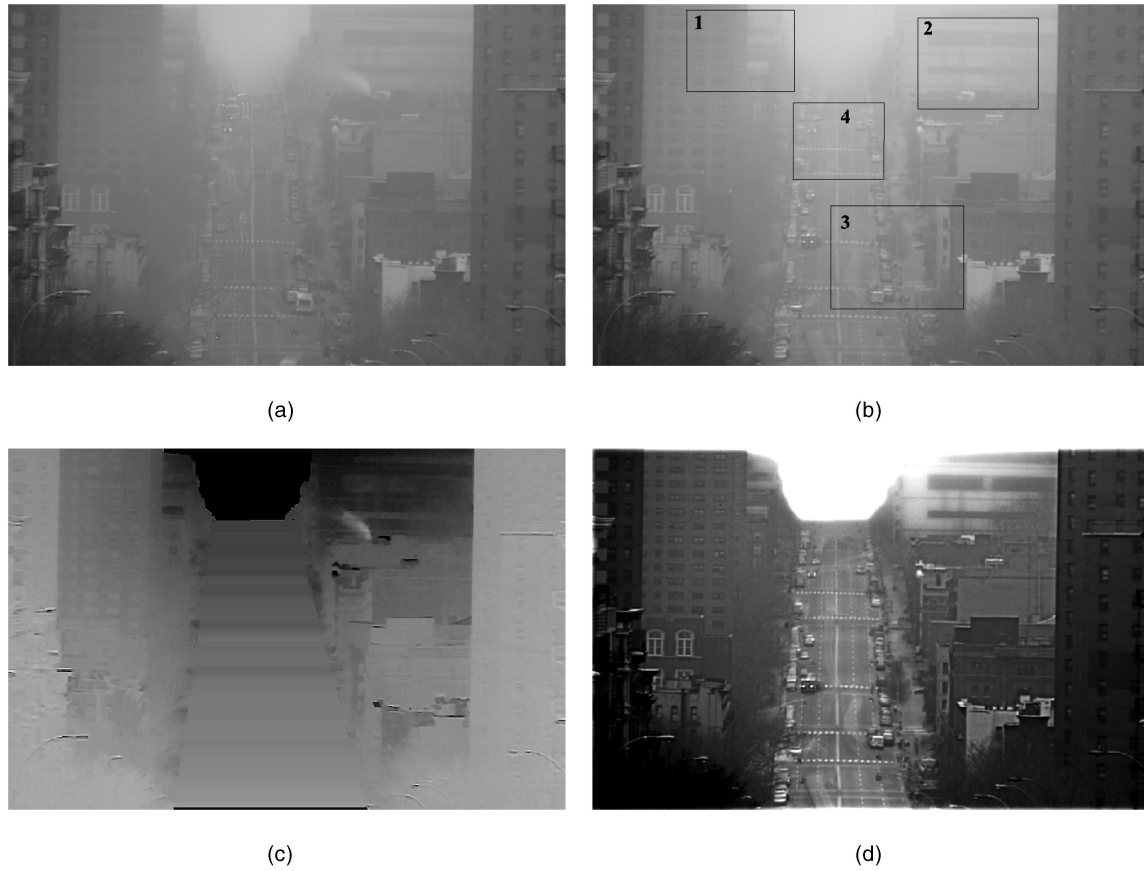


Fig. 10. (a) Scene imaged at 5:00 P.M. (b) Scene imaged at 5:30 P.M. (c) Depth map computed from images (a) and (b). (d) Contrast restored using image (b). Experiments with videos of a traffic scene on a foggy day. (a) and (b) Two short video clips were captured half an hour apart using an 8-bit video camera. 100 frames were averaged to reduce noise. Note that the vehicles on the road in the two images are different. (c) The depth map was computed for the background image using the algorithm presented in Section 5. The scaled depths of the region corresponding to the road were linearly interpolated using scaled depth values at pixels on the left and right corners of the road. (d) The defogged (contrast restored) image obtained from the video frame in (b). Compare the contrast restored image with the histogram equalized image in Fig. 12.

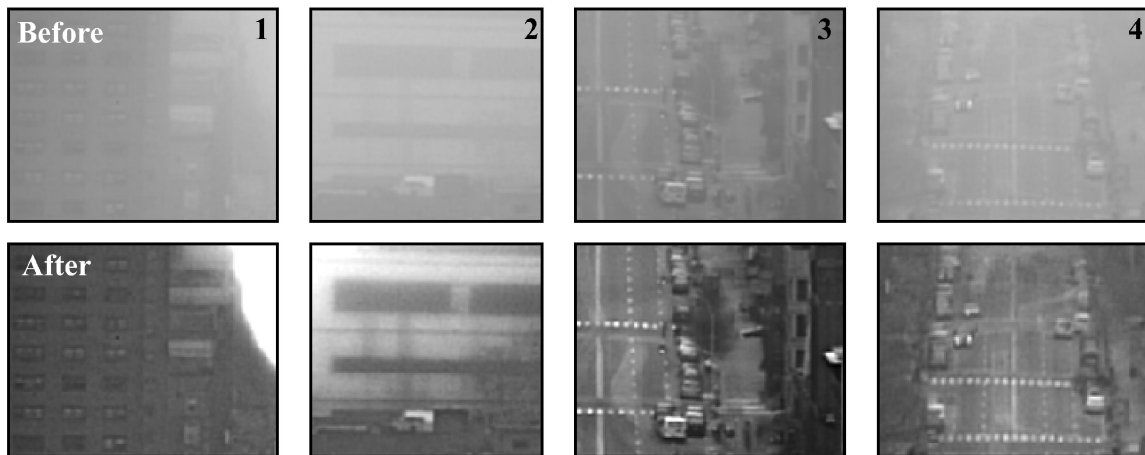


Fig. 11. Zoomed in regions of the frame (see the marked rectangles in Fig. 10b) demonstrate the significant increase in contrast at various depths of the scene. Note that different amounts of fog were removed at different depths. Also, notice the better contrast of moving objects (vehicles).

black and white camera (entire visible range), or smaller color bands (R, G, B) for a color camera, or narrow band multi-spectral cameras. Thus, for removal of fog and dense haze, we can use RGB color or gray-scale cameras whereas we must use narrow spectral band cameras for the removal of many aerosols.

ACKNOWLEDGMENTS

This work was supported in part by a DARPA/ONR HumanID Contract (N00014-00-1-0916) and an US National Science Foundation Award (IIS-99-87979). The authors thank Yoav Schechner for valuable discussions on this topic. Some of the results presented in this paper have appeared in the



Fig. 12. Artificial contrast enhancement (not contrast restoration) of a foggy image by histogram equalization does not remove fog completely at all depths in the scene. In this example, farther depths have poorer contrast when compared to the nearer depths.

Proceedings of the 2001 IEEE Conference on Computer Vision and Pattern Recognition [22].

REFERENCES

- [1] T.E. Boult and L.B. Wolff, "Physically-Based Edge Labelling," *Proc. IEEE Conf. Computer Vision and Pattern Recognition*, 1991.
- [2] B. Cairns, B.E. Carlson, A.A. Lacis, and E.E. Russell, "An Analysis Of Ground-Based Polarimetric Sky Radiance Measurements," *Proc. SPIE*, vol. 3121, 1997.
- [3] S. Chandrasekhar, *Radiative Transfer*. Dover Publications, Inc., 1960.
- [4] D.B. Chenault and J.L. Pezzaniti, "Polarization Imaging through Scattering Media," *Proc. SPIE*, vol. 4133, 2000.
- [5] K.L. Coulson, "Polarization of Light in the Natural Environment," *Proc. SPIE*, vol. 1166, 1989.
- [6] L.J. Denes, M. Gottlieb, B. Kaminsky, and P. Metes, "Aotf Polarization Difference Imaging," *Proc. SPIE*, vol. 3584, 1998.
- [7] S.D. Gedzelman, "Atmospheric Optics in Art," *Applied Optics*, vol. 30, 1991.
- [8] J. Gordon and P. Church, "Overcast Sky Luminances and Directional Luminous Reflectances of Objects and Backgrounds under Overcast Skies," *Applied Optics*, vol. 5, p. 919, 1966.
- [9] L.L. Grewe and R.R. Brooks, "Atmospheric Attenuation Reduction through Multisensor Fusion," *Sensor Fusion: Architectures, Algorithms, and Applications II*, *Proc. SPIE*, vol. 3376, Apr. 1998.
- [10] Van De Hulst, *Light Scattering by Small Particles*. John Wiley and Sons, 1957.
- [11] R.L. Lee Jr., "Horizon Brightness Revisited: Measurements and a Model of Clear-Sky Radiances," *Applied Optics*, vol. 20, pp. 4620-4628, 1994.
- [12] N.S. Kopeika, "General Wavelength Dependence of Imaging through the Atmosphere," *Applied Optics*, vol. 20, no. 9, May 1981.
- [13] N.S. Kopeika, *A System Engineering Approach to Imaging*. SPIE Press, 1998.
- [14] D.K. Lynch, "Step Brightness Changes of Distant Mountain Ridges and Their Perception," *Applied Optics*, vol. 30, 1991.
- [15] S. Mahadev and R.C. Henry, "Color Perception through Atmospheric Haze," *J. Optical Soc. Am. A*, vol. 17, no. 5, May 2000.
- [16] E.J. McCartney, *Optics of the Atmosphere: Scattering by Molecules and Particles*. John Wiley and Sons, 1975.
- [17] W.E.K. Middleton, *Vision through the Atmosphere*. Univ. of Toronto Press, 1952.
- [18] M. Minnaert, *The Nature of Light and Color in the Open Air*. Dover Publications, Inc., 1954.
- [19] T. Mitsunaga and S.K. Nayar, "Radiometric Self Calibration," *Proc. IEEE Conf. Computer Vision and Pattern Recognition*, 1999.
- [20] P. Moon and D.E. Spencer, "Illumination from a Non-Uniform Sky," *Illuminating Eng.*, vol. 37, pp. 707-726, 1942.
- [21] S.G. Narasimhan and S.K. Nayar, "Chromatic Framework for Vision in Bad Weather," *Proc. IEEE Conf. Computer Vision and Pattern Recognition*, 2000.
- [22] S.G. Narasimhan and S.K. Nayar, "Removing Weather Effects from Monochrome Images," *Proc. IEEE Conf. Computer Vision and Pattern Recognition*, 2001.
- [23] S.G. Narasimhan and S.K. Nayar, "Vision and the Atmosphere," *Int'l J. Computer Vision*, vol. 48, no. 3, pp. 233-254, Aug. 2002.
- [24] S.K. Nayar and S.G. Narasimhan, "Vision in Bad Weather," *Proc. Seventh Int'l Conf. Computer Vision*, 1999.
- [25] J.P. Oakley and B.L. Satherley, "Improving Image Quality in Poor Visibility Conditions Using a Physical Model for Degradation," *IEEE Trans. Image Processing*, vol. 7, Feb. 1998.
- [26] "Museum of Science," Leonardo's Perspective. <http://www.mos.org/sln/Leonardo/InvestigatingAerialP.html>, 1997.
- [27] M.J. Rakovic, G.W. Kattawar, M. Mehrubeoglu, B.D. Cameron, L.V. Wang, S. Rastegar, and G.L. Cote, "Light Backscattering Polarization Patterns from Turbid Media: Theory and Experiment," *Applied Optics*, vol. 38, 1999.
- [28] M.P. Rowe, E.N. Pugh Jr., J.S. Tyo, and N. Engheta, "Polarization-Difference Imaging: A Biologically Inspired Technique for Observation through Scattering Media," *Optical Letters*, vol. 20, 1995.
- [29] Y.Y. Schechner, S.G. Narasimhan, and S.K. Nayar, "Instant Dehazing of Images Using Polarization," *Proc. IEEE Conf. Computer Vision and Pattern Recognition*, 2001.
- [30] Y.Y. Schechner, S.G. Narasimhan, and S.K. Nayar, "Polarization Based Vision through Haze," *Applied Optics*, special issue: light and color in the open air, vol. 42, no. 3, Jan. 2003.
- [31] S. Shafer, "Using Color to Separate Reflection Components," *Color Research and Applications*, pp. 210-218, 1985.
- [32] C. Stauffer and W.E.L. Grimson, "Adaptive Background Mixture Models for Real-Time Tracking," *Proc. IEEE Conf. Computer Vision and Pattern Recognition*, 1999.
- [33] K. Tan and J.P. Oakley, "Enhancement of Color Images in Poor Visibility Conditions," *Proc. Int'l Conf. Image Processing*, vol. 2, Sept. 2000.
- [34] K. Tan and J.P. Oakley, "Physics Based Approach to Color Image Enhancement in Poor Visibility Conditions," *J. Optical Soc. Am. A*, vol. 18, no. 10, pp. 2460-2467, Oct. 2001.
- [35] S. Ullman, "On the Visual Detection of Light Sources," *Biological Cybernetics*, pp. 205-212, 1976.
- [36] J.G. Walker, P.C.Y. Chang, and K.I. Hopcraft, "Visibility Depth Improvement in Active Polarization Imaging in Scattering Media," *Applied Optics*, vol. 39, 1995.
- [37] W.L. Wolfe and G.J. Zissis, *The Infrared Handbook*. Prepared for Office of Naval Research, Dept. of the Navy, 1978.
- [38] Y. Yitzhaky, I. Dror, and N.S. Kopeika, "Restoration of Atmospherically Blurred Images According to Weather-Predicted Atmospheric Modulation Transfer Function," *Optical Eng.*, vol. 36, Nov. 1998.



Srinivasa G. Narasimhan received the MS degree in computer science from Columbia University in 1999. He is currently pursuing the PhD degree in computer science at the Columbia University Vision Laboratory. His research is focused on the development of physics-based models and algorithms for scene understanding in bad weather. His paper received the Best Paper Honorable Mention Award at the 2000 IEEE Computer Vision and

Pattern Recognition Conference.



Shree K. Nayar received the PhD degree in electrical and computer engineering from the Robotics Institute at Carnegie Mellon University in 1990. He is the T.C. Chang Professor of Computer Science at Columbia University. He currently heads the Columbia Automated Vision Environment (CAVE), which is dedicated to the development of advanced computer vision systems. His research is focused on three areas, namely, novel vision sensors, physics-based

models for vision, and algorithms for scene understanding. His work is motivated by applications in the fields of computer vision, computer graphics, human-machine interfaces, and robotics. Dr. Nayar has authored and coauthored papers that have received the Best Paper Honorable Mention Award at the 2000 IEEE Computer Vision and Pattern Recognition Conference (CVPR), the David Marr Prize at the 1995 International Conference on Computer Vision (ICCV) held in Boston, Siemens Outstanding Paper Award at the 1994 IEEE CVPR Conference held in Seattle, the 1994 Annual Pattern Recognition Award from the Pattern Recognition Society, Best Industry Related Paper Award at the 1994 International Conference on Pattern Recognition held in Jerusalem, and the David Marr Prize at the 1990 ICCV held in Osaka. He holds several US and international patents for inventions related to computer vision and robotics. He was the recipient of the David and Lucile Packard Fellowship for Science and Engineering in 1992, the National Young Investigator Award from the US National Science Foundation in 1993, and the Excellence in Engineering Teaching Award from the Keck Foundation in 1995.

▷ **For more information on this or any other computing topic, please visit our Digital Library at <http://computer.org/publications/dlib>.**